The energy flow analysis as a tool for identification of damping in tall buildings subjected to wind

Contributions of the foundation and the building structure

Gómez, S. S.; Metrikine, A. V.

DOI
10.1115/1.4040975

Publication date
2019

Document Version
Final published version

Published in
Journal of Vibration and Acoustics, Transactions of the ASME

Citation (APA)
Gómez, S. S., & Metrikine, A. V. (2019). The energy flow analysis as a tool for identification of damping in tall buildings subjected to wind: Contributions of the foundation and the building structure. *Journal of Vibration and Acoustics, Transactions of the ASME*, *141*(1), Article 011013. https://doi.org/10.1115/1.4040975

The Energy Flow Analysis as a Tool for Identification of Damping in Tall Buildings Subjected to Wind: Contributions of the Foundation and the Building Structure

S. S. Gómez
Faculty of Civil Engineering and Geosciences,
Department of Structural Engineering,
Delft University of Technology,
Stevinweg 1,
Delft 2628CN, The Netherlands;
TNO Structural Dynamics,
Leeghwaterstraat 44,
Delft 2628CA, The Netherlands
e-mail: s.anchezgomez-1@tudelft.nl

A. V. Metrikine
Faculty of Civil Engineering and Geosciences,
Department of Structural Engineering,
Delft University of Technology,
Stevinweg 1,
Delft 2628CN, The Netherlands
e-mail: A.Metrikine@tudelft.nl

In this paper, the energy dissipated in a tall building is identified by means of the energy flow analysis. This approach allows assessing energy dissipation within a specific domain or element of the structure. In this work, the focus is placed on the superstructure, which is the part of the building above the ground, and on the foundation. Damping operators for the superstructure and the foundation are formulated based on the identified energy dissipation in these parts of the building. The obtained damping operators are used to compute the modal damping ratios in a simplified model of the building. The modal damping ratios of the three lowest modes of vibration are compared to those identified in full-scale measurements by means of the half-power bandwidth method.
[DOI: 10.1115/1.4040975]

1 Introduction

At present, buildings are getting taller, lighter, and more slender making them sensitive to the dynamic loads such as wind. For such structures, the serviceability limit state is the limiting design factor, which affects the comfort of the building occupants. In order to reduce the discomfort caused by wind-induced vibrations, the dynamic behavior of building structures should improve. This behavior is strongly influenced by its mass, stiffness, and damping of the building. There are numerous software packages that can reproduce the stiffness and the mass accurately. On the contrary, damping cannot yet be accurately reproduced due to the complexity of the underlying physical processes causing the energy dissipation. Consequently, estimates based on the type of the building material, or predictions based on identified damping values of existing structures [1–4] are used to form the input to the numerical models of tall structures. Given that, and due to the fact that tall structures cannot be tested prior to construction, it often happens that the acceleration level of the erected construction is perceptibly larger than the predicted one. This causes undesirable discomfort to occupants of the building. Therefore a more accurate and detailed prediction of damping in tall buildings is required.

Fundamentally, damping is understood as the capacity of a system to dissipate energy. It is well known that there are three major energy dissipation mechanisms, namely damping in the building structure, the dynamic interaction of the building foundation and the soil, and the aerodynamic damping [4]. It is therefore of a paramount importance to identify the contribution of these energy dissipation mechanisms to the total energy dissipation in the buildings.

Modal properties of building structures such as modal damping can be studied by means of the powerful and well-established modal-based analysis [5–7]. These techniques help to identify equivalent linear damping of a structure, and when a sufficient number of modes are involved in the analysis, the deformation field at a specific location in the structure can be accurately modeled. It needs to be noted, however, that wind excites only a few lowest modes of the building, which limits the applicability of the modal-based identification techniques. For this reason, it is desirable to develop a dissipation identification technique, which is not based on the modal analysis.

In this paper, a recently developed method [8,9] based on the energy flow analysis for damping identification is applied to a full-scale structure located in The Netherlands. An advanced beam model is used to account for the three-dimensional effects character of the building motion.

As stated previously, in a building, there are three major energy dissipation mechanisms that can be distinguished. Noting that in tall structures, aerodynamic damping is negligible, the focus in this paper is placed on the foundation damping and damping in the structure. Both are identified by means of the energy flow analysis [10–20].

The paper is organized as follows: In Sec. 2, the full-scale measurements are described in detail. In Sec. 3, the energy flow method is used in conjunction with the adopted beam model in order to identify the amount of dissipated energy in the building and in the foundation. In Sec. 4, effective viscous damping coefficients for the building and the foundation are deduced from the identified dissipated energy. In Sec. 5, the modal damping corresponding to the deduced effective damping coefficients is derived and compared to those identified directly from the full-scale measurements. Conclusions to the study are offered in Sec. 6.

2 Full-Scale Measurements of Wind-Induced Vibrations

2.1 Building Description. The JuBi tower (Fig. 1) is a 146 m office building with 39 storys located in The Netherlands. The JuBi tower is a concrete tube in tube structure.

The horizontal stability of the building is provided by the three internal concrete cores of a rectangular shape and the outside

Contributed by the Technical Committee on Vibration and Sound of ASME for publication in the Journal of Vibration and Acoustics. Manuscript received February 1, 2018; final manuscript received July 19, 2018; published online September 10, 2018. Assoc. Editor: Jeffrey F. Rhoads.

Fig. 1 The JuBi tower

walls of an asymmetric shape. The storys are separated by lightweight floors hinged to the outside walls and to the internal cores. Therefore, the floors do not significantly contribute to the horizontal resistance of the building. Vertical loads on the floors are transferred to the cores and the outside walls, and then directly to the foundation. The building is located on a soft soil.

2.2 Soil Conditions. Prior to the construction of the building, soil characteristics of the site were identified by means of the cone penetration test tests at several locations within the foundation boundaries.[1] A cone penetration test (CPT) test employs a cone that penetrates into the soil measuring the resistance of the soil. Data recorded by means of the CPT test cannot be directly used for calculations. However, shear wave speed, which is a relevant parameter to compute soil resistance can, be calculated based on recorded data of a CPT test making use of the most appropriate correlation [21–24]. The identification of the soil shear wave speed helps us to describe the characteristics of soil layers up to certain depth. This depth usually extends to at least the foundation pile length. Given that, the soil-foundation resistance can be identified.

At the location of the JuBi tower, several CPT tests were performed. The shear wave speeds identified by means of Robertson's correlation [24] from these measurements are depicted in Fig. 2. Looking at Fig. 2, three distinct soil layers can be identified, and the mean shear wave speed at each layer is plotted (black dashed line). Moreover, it can be noted that the shear wave speed is relatively low. This is rather common for soft-soil conditions typically found in The Netherlands.

2.3 Instrumentation and Field Measurements. Acceleration and strain measurements were carried out in the JuBi tower under strong wind conditions as shown in Fig. 3. Accelerations at the 9th, 22nd, and 37th floors and strains at the 9th floor were recorded during 2 h. Figure 3 shows the measurement strategy used during the measurement campaign. This instrumentation strategy is chosen such as to collect the information needed for the energy flow analysis.

The 37th floor is instrumented with four accelerometers. Accelerometers 5, 7, and 8 are placed such that accelerations in the weak direction (Y-direction) are registered. Accelerometer 6 is placed 90 degrees with respect to accelerometer 5 in order to measure accelerations in the stiff direction (Z-direction). Making use of accelerometer 5 in combination with accelerometer 8 the torsional motion can be measured. This instrumentation disposition also allows us to identify the global fundamental modes, in the weak and stiff translational directions as well as in the torsional direction of the building structure. At the 22nd floor, accelerometers 3 and 4 are placed perpendicular to each other to measure accelerations in the weak and stiff translational directions. At the 9th floor, strains and accelerations are measured. Accelerometers 1 and 2 shown in Fig. 3 are placed using the same strategy as used to instrument the other floors. On the same floor, 24 strain gauges are mounted on the various components (cores, piles, and outside walls) in order to map the strain distribution. Besides, several strain gauges are installed on different components in a rosette shape.

The data acquisition system (DAQ) and instrumentation used during the measurements are described in Table 1.

Acceleration and strain data were recorded in subsamples of 10 min. After some data processing, time traces of each accelerometer are transformed to the frequency domain for identification purposes.

The power spectral density (PSD) of the velocity is shown in Fig. 4. In order to obtain velocity signals, the acceleration is integrated numerically and then the mean value of the resulting dependence of the velocity on time is set to zero. The figure shows that all accelerometers record signals at all resonance frequencies. This means that the directional placement of the accelerometers does not correspond to the principal directions of the modal vibrations. This is prohibitive for the direct identification of the modal damping. In order to deal with this inconvenience, the acceleration signals were manipulated making use of rigid body kinematics described in the following equation:

$$\mathbf{v}_B = \mathbf{v}_A + \boldsymbol{\Omega} \times \mathbf{r}_A^B \tag{1}$$

Assuming that each floor behaves as a rigid body (the assumptions used in this paper are listed in the Appendix), the velocity at any point $\mathbf{v}_B$ can be computed as the velocity at a certain point $\mathbf{v}_A$ plus the angular velocity $\boldsymbol{\Omega}$ times the distance between A and B. By

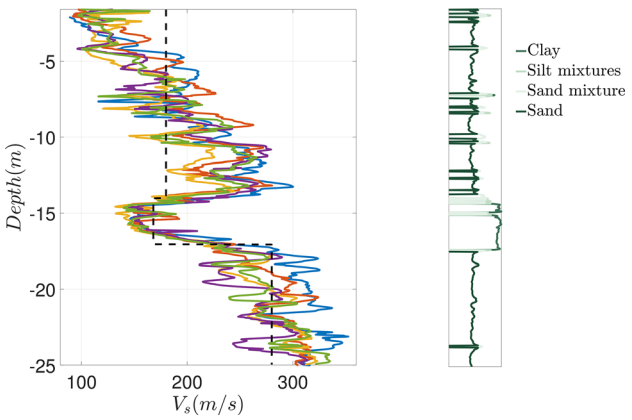

Fig. 2 The soil shear wave speed at the location of the JuBi tower

[1] https://www.dinoloket.nl/.

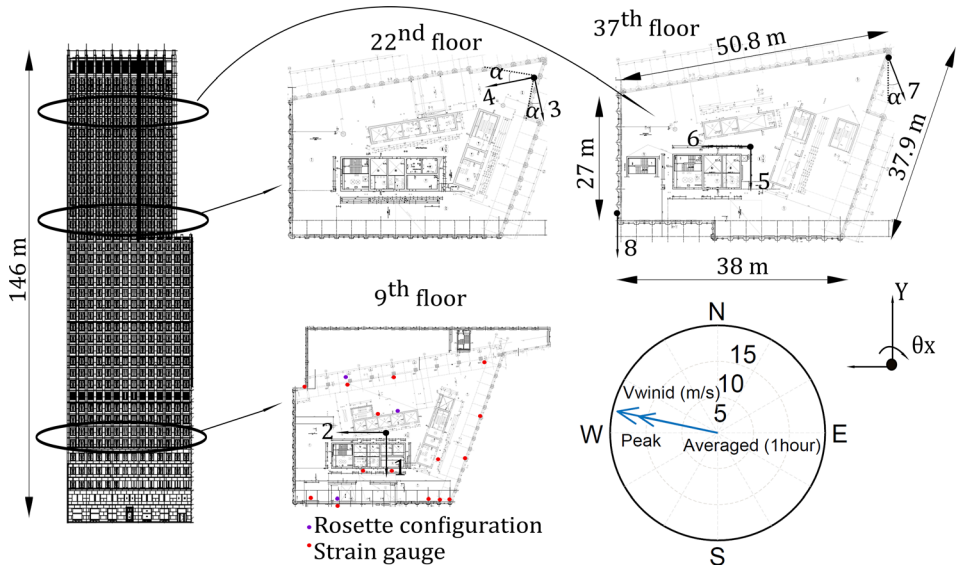

Fig. 3 The instrumentation configuration at the 9th, 22nd, and 37th floors

Table 1 DAQ and instrumentation description

Equipment	Model	Software and characteristics
DAQ 9th floor DAQ 22nd floor and 37th floor	HBM-MGCplus(MGC5) Dewetron DEWE-50-USB-8	Catman 4.0.3 Dewesoft 7.1.1 Sampling frequency 100 Hz Range ±10 mV/V and 20 m/s Voutput = 9.81 V
Accelerometers	Sundstrand QA-700 (×8)	Amplifier: DAQP STG Filter Butterworth: 10 Hz Sensitivity 30 g/N Sampling frequency 100 Hz Range 2000 mV/V Resistance 120±0.3Ω
Strain gauges	Tokyio Sokki PL-60-11 (×24)	Amplifier: ML801 Filter Butterworth: 10 Hz Half bridge Bridge factor 1 Gauge factor 2.13

means of Eq. (1), single-mode signals can be computed as shown in Fig. 5.

Once the modes are separated, single degree-of-freedom-based identification techniques can be applied to the signals. Looking at Fig. 5, one can notice that the spectral density functions of the translational signals (Y- and Z-directions) show double peaks. It is tempting to conclude that these peaks correspond to two distinct global modes, which correspond to specific shapes of vibrations of the building as a whole. This is not the case though. The true reason for these peaks is that the JuBi tower consists of three cores and the outer walls, which have close natural frequencies as can be deduced from the strain measurement data. The cores and the walls are coupled by the floors but only weakly. Therefore, the

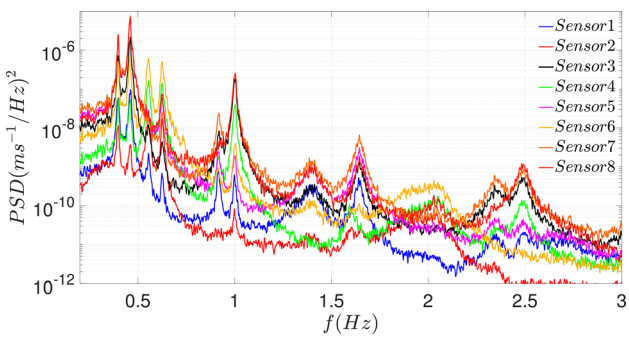

Fig. 4 The PSD functions at the 9th, 22nd, and 37th floors

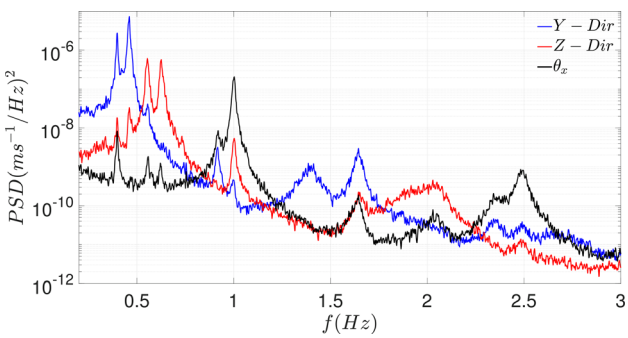

Fig. 5 The PSD functions of the shifted signals at the 37th floor

two closely spaced peaks shown in Fig. 5 correspond to the slightly modified natural frequencies of the cores and the walls.

In this work, the half-power bandwidth method (HPBW) [25] is applied to the data shown in Fig. 5 to identify the fundamental frequencies f_n and the corresponding equivalent viscous damping ratios ξ_n for the three fundamental modes of the building (two translational and one rotational around the vertical axis).

Due to the fact that the JuBi tower has two closely spaced resonant frequencies, using the HPBW method for damping identification becomes not straightforward. Therefore, given that these two resonant frequencies correspond to the components of a weakly coupled system, an equivalent viscous damping ratio at each peak has been identified and averaged. For the torsional mode, no such behavior is identified. Consequently, the HPBW method can be directly applied to the latter. It should be noted that the experimentally identified equivalent viscous damping ratios are not true damping values for the assumed real-valued modes given the fact that these modes are coupled. However, in this work, the HPBW method is used to give an indication of the effective damping ratio, which is used for comparison with the damping values identified by the energy flow method. The averaged damping ratios identified by means of the HPBW method are presented in Table 2.

Figure 6 shows the damping identified by means of the HPBW method at one of the peaks of the two translational PSD functions and the torsional one. The equivalent viscous damping in each peak is computed by means of the following expression.

$$2\xi = \frac{\Delta f}{f_n} \tag{2}$$

where f_n accounts for the fundamental frequency, and Δf accounts for the frequency distance at half of the height of the spike.

3 Model and Energy Flow Analysis

The energy flow analysis is used in this work to identify the energy dissipated in a full-scale structure. During vibration of a high-rise building, not only the part of the structure above the ground level (superstructure) moves but also the surrounding soil and the foundation. This entails that in the course of the building vibration, energy is dissipated both in the superstructure and the foundation due to the interaction with the soil [26]. The soil–structure interaction (SSI) is rather complex and sometimes uncertain, and it is commonly named SSI [27–29]. Although the SSI is a process, which takes place beneath ground level, the superstructure can strongly influence the SSI effects and vice versa. Modeling the dynamic SSI for high-rise buildings is a quite challenging task due to uncertainties in the characteristic of the soil properties as well as the complexity of the foundation system. Especially challenging is the prediction of the dissipative properties of the building structure and the SSI-associated damping. Therefore, in this work, a novel method for damping identification based on the energy flow analysis is used to identify the dissipative properties of a high-rise building in full-scale. Additionally, an attempt is made to identify the energy dissipated in the superstructure separately from that dissipated in the soil–foundation interaction.

3.1 Beam Model and Energy Flow Analysis. In order to study the energy dissipated in the JuBi tower subject to wind loads by means of the energy flow analysis an Euler–Bernoulli beam

Table 2 Comparison between identified damping and calculated by means of the energy flow analysis

	Identified (averaged)	Energy method
ξ_y	1.0%	1.1%
ξ_z	1.2%	2.0%
ξ_{θ_x}	0.73%	1.2%

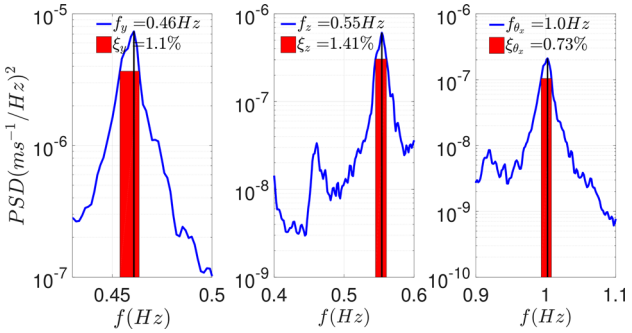

Fig. 6 The HPBW method applied to the shifted signals at the 37th floor

model is adopted. The tower is sketched in Fig. 7. Its stability is assured by three concrete cores and the outer walls as shown in Fig. 7.

It can be noted from Fig. 7 that the structure has a complex and asymmetric shape. This, in combination with the random load distribution given by the wind gusts, makes it reasonable to assume that during the vibration the building performs both translational and torsional vibrations which are coupled.

In order to account for these motions and their coupling in a relatively simple manner for this specific building, an appropriate beam model is developed as described below.

It is assumed that the cross section perpendicular to the largest dimension of the beam (building) remains plane after deformation. This means that the cross section of the beam moves as a rigid body and is uniquely described by a position vector $\mathbf{w} = [w_x\ w_y\ w_z]$ and a rotation vector $\boldsymbol{\theta} = [\theta_x\ \theta_y\ \theta_z]$, where x, y, and z are the components of the coordinate system. Further, geometrical linearity is assumed, implying the angles of rotation to be small. Now, taking as a reference a material point in the cross section, a displacement vector $\mathbf{u} = \mathbf{u}(x, y, z, t)$ with the components u_x, u_y, and u_z is described as follows:

$$\begin{aligned} u_x(x,y,z,t) &= w_x(x,t) + z\theta_y(x,t) - y\theta_z(x,t) \\ u_y(x,y,z,t) &= w_y(x,t) - z\theta_x(x,t) \\ u_z(x,y,z,t) &= w_z(x,t) + y\theta_x(x,t). \end{aligned} \tag{3}$$

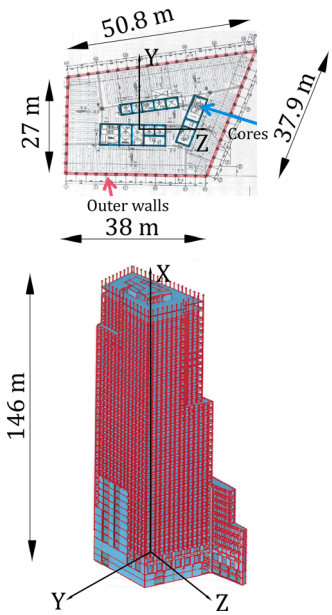

Fig. 7 Layout of the stability cores and walls of the JuBi tower

The corresponding strain components read

$$\epsilon_{xx} = \frac{\partial u_x}{\partial x};\ \gamma_{xy} = \frac{\partial u_x}{\partial y} + \frac{\partial u_y}{\partial x};\ \gamma_{xz} = \frac{\partial u_x}{\partial z} + \frac{\partial u_z}{\partial x} \tag{4}$$

The equations of motion will be formulated employing the Lagrangian formalism. In general, the Lagrangian of a conservative system reads

$$\mathscr{L} = \mathscr{K} - \mathscr{V} \tag{5}$$

where $\mathscr{K} = \int_0^L K(\dot{u}, \dot{u}')\mathrm{d}x$ and $\mathscr{V} = \int_0^L V(u, u', u'')\mathrm{d}x$ are the kinetic and potential energy, respectively. Therefore, the Lagrangian density function can be express in a general manner as $\lambda = \lambda(u, u', u'', \dot{u}, \dot{u}')$, where the Lagrangian reads as

$$\begin{aligned}\mathscr{L} = \int_0^L \lambda(x,t)\mathrm{d}x = \int_0^L \Bigg\{ &\left(\frac{1}{2}\rho A\left(\left(\dot{w}_x(x,t) + z\dot{\theta}_y(x,t) - y\dot{\theta}_z(x,t)\right)^2 + \left(\dot{w}_y(x,t) - z\dot{\theta}_x(x,t)\right)^2 + \left(\dot{w}_z(x,t) + y\dot{\theta}_x(x,t)\right)^2\right)\right) \\ &-\Bigg(-T(x)w_x'^2 + \frac{1}{2}E(x)\Big(Aw_x'^2(x,t) - 2S_y w_x'(x,t)w_z''(x,t) - 2S_z w_x'(x,t)w_y''(x,t) + 2S_\omega w_x'(x,t)\theta_x''(x,t) \\ &+ I_{yy}w_z''^2(x,t) + 2I_{yz}w_z''(x,t)w_y''(x,t) - 2I_{z\omega}w_z''(x,t)\theta_x''(x,t) + I_{zz}w_y''^2(x,t) - 2I_{y\omega}w_y''(x,t)\theta_x''(x,t) + I_\omega\theta_x''^2(x,t)\Big) + \frac{1}{2}G(x)K\theta_x'^2(x,t)\Bigg\}\mathrm{d}x\end{aligned} \tag{6}$$

The Euler–Lagrange equation for one-dimensional systems can be described in its general form as follows:

$$\frac{\partial\lambda}{\partial u_i} - \frac{\partial}{\partial t}\frac{\partial\lambda}{\partial\dot{u}_i} + \frac{\partial}{\partial x}\frac{\partial\lambda}{\partial u_i'} + \frac{\partial^2}{\partial x^2}\frac{\partial\lambda}{\partial u_i''} + \frac{\partial^2}{\partial t\partial x}\frac{\partial\lambda}{\partial\dot{u}_i\partial u_i'} + \bar{Q} = 0 \tag{7}$$

Where u_i denotes the generalized coordinate at each direction $i = x$, y, and z. Now, substituting the Lagrangian function described in Eq. (6) into the Euler–Lagrange equation Eq. (7), equations of motion that govern small vibrations of the coupled system represented in Fig. 7 are obtained

$$\left(\sum_{j=1}^{N_{\text{floors}}}\frac{M_j}{L} + \sum_{k=1}^{N_{\text{cores}}}\rho_k A_k\right)\left(\ddot{w}_y(x,t) - z\ddot{\theta}_x(x,t)\right) + \sum_{k=1}^{N_{\text{cores}}} T_k(x)w_y''(x,t) - ES_z^k w_x'''(x,t) + EI_{yz}^k w_z''''(x,t) + EI_{zz}^k w_y''''(x,t) = F_y(x,t) \tag{8}$$

$$\left(\sum_{j=1}^{N_{\text{floors}}}\frac{M_j}{L} + \sum_{k=1}^{N_{\text{cores}}}\rho_k A_k\right)\left(\ddot{w}_z(x,t) + y\ddot{\theta}_x(x,t)\right) + \sum_{k=1}^{N_{\text{cores}}} T_k(x)w_z''(x,t) - ES_y^k w_x'''(x,t) + EI_{zy}^k w_y''''(x,t) + EI_{yy}^k w_z''''(x,t) = F_z(x,t) \tag{9}$$

$$\left(\sum_{j=1}^{N_{\text{floors}}}\frac{M_j}{L} + \sum_{k=1}^{N_{\text{cores}}}\rho_k I_p^k\right)\ddot{\theta}_x(x,t) + \sum_{k=1}^{N_{\text{cores}}}\rho_k A_k y\ddot{w}_z(x,t) - \rho_k A_k z\ddot{w}_y(x,t) + G_k K_k\theta_x''(x,t) = F_x(x,t) \tag{10}$$

Where

$$T_k(x) = \int_L \rho A g(L-x)\mathrm{d}x \tag{11}$$

Equation (8) describes the equilibrium in Y-direction (weak direction of the building), Eq. (9) represents the equilibrium in Z-direction (stiff direction) and Eq. (10) describes the dynamic torque about X-axis.

The Lagrangian formalism can also be used to formulate the energy balance equation, which has the following form:

$$\frac{\mathrm{d}}{\mathrm{d}t}E(t) + S(x,t)\Big|_{L_{\text{initial}}}^{L_{\text{final}}} = W_{\text{ext}}(t) - W_{\text{diss}}(t) \tag{12}$$

where $E(t)$ is the energy change obtained by the summation of the kinetic and the potential energy described in Eqs. 13 and 14

$$\mathscr{K} = \frac{1}{2}\int_L\left\{\rho\int_A\left(\dot{u}_x^2 + \dot{u}_y^2 + \dot{u}_z^2\right)dA\right\}\mathrm{d}x \tag{13}$$

and

$$\mathscr{V} = \frac{1}{2}\int_L\left\{E\int_A\epsilon_{xx}^2 dA\right\}\mathrm{d}x + \frac{1}{2}\int_L\left\{G\int_A\left(\gamma_{xy}^2 + \gamma_{xz}^2\right)\mathrm{d}A\right\}\mathrm{d}x \tag{14}$$

S is the energy flow at specific boundaries L_{final} and L_{initial}. The energy flow is computed by means of the following equation:

$$S(x,t) = \left(\frac{\partial u_i}{\partial t}, \frac{\partial \lambda}{\partial u_i'} - \frac{\partial}{\partial x}\frac{\partial \lambda}{\partial u_i''} - \frac{\partial}{\partial t}\frac{\partial \lambda}{\partial u_i' \partial \dot{u}_i}\right) + \left(\frac{\partial^2 u_i}{\partial x \partial t}, \frac{\partial \lambda}{\partial u_i''}\right) \tag{15}$$

The W_{diss} is the rate of energy dissipated within the boundaries (L_{initial} to L_{final}) and W_{ext} are the rate of energy introduced to the system by external forces. Equation (12) shows that the energy change in the system is balanced by (i) the energy flow S through specific boundaries, (ii) the energy dissipated W_{diss}, and (iii) the external effects W_{ext}. Now, introducing the Fourier transform pair as

$$\tilde{F}_n(\omega) = \mathscr{F}(f_n(t)) = \int_{-\infty}^{\infty} f_n(t) e^{-i\omega t} dt \quad \text{and}$$
$$f_n(t) = \mathscr{F}^{-1}\left(\tilde{F}_n(\omega)\right) = \frac{1}{2\pi}\int_{-\infty}^{\infty} \tilde{F}_n(\omega) e^{i\omega t} d\omega. \tag{16}$$

The energy balance equation Eq. (12) of a time interval $[t;\ t+T]$ is transformed into the frequency domain as shown in Eq. (17)

$$\int_{-\infty}^{\infty} \left\{ E(\tilde{t})|_t^{t+T} + \int_t^{t+T} S(x,\tilde{t})|_{L_{\text{initial}}}^{L_{\text{final}}} d\tilde{t} \right\} e^{-i\omega t} dt$$
$$= \int_{-\infty}^{\infty} \left\{ \int_t^{t+T} W_{\text{ext}}(\tilde{t}) d\tilde{t} - \int_t^{t+T} W_{\text{diss}}(\tilde{t}) d\tilde{t} \right\} e^{-i\omega t} dt \tag{17}$$

where the energy change $E(\tilde{t})$ and the energy flow $S(x,\tilde{t})$ are first numerically integrated over a time span $[t;\ t+T]$ and then transformed to the frequency domain making use of the fast Fourier transform.

3.2 Energy Dissipation in the Superstructure of the JuBi Tower Subject to Wind. In this section, Eq. (17) and the data recorded during the measurement campaign are used in order to identify the energy dissipation in the structure. As described in Sec. 2.3, the measurements were performed at three levels of the building. In order to compute the energy dissipated in the superstructure, data recorded at the top level L_f (37th floor) and at the bottom level L_l (9th floor) in combination with the energy balance equation are used. The energy change term in Eq. (17) is computed using the following formula:

$$E(\tilde{t})|_t^{t+T} = \frac{(L_f - L_l)}{2}\left(\tilde{e}_l(\tilde{t}) + \tilde{e}_f(\tilde{t})\right)|_t^{t+T} \tag{18}$$

where $\tilde{e}_l(\tilde{t})$ is the energy density computed at the bottom of the superstructure and $\tilde{e}_f(\tilde{t})$ is the energy density at the top measurement location of the superstructure. At the top level, the kinetic energy is computed in accordance with Eq. (13) and using the accelerometer data. It is assumed that the elastic energy density, as well as the energy flow at the top of the building, is negligible in comparison with the kinetic energy so that the top level is characterized solely by the kinetic energy. At the bottom level, the kinetic and the elastic energy are computed in accordance with Eqs. (13) and 14 using the recorded strain and acceleration data. Several strain gauges were glued around each of the cores and the outer walls of the building; therefore, the elastic energy is computed at each core and the outer walls and added together. The energy flow crossing the bottom level L_l is also computed. This concludes the quantification of the left-hand side of Eq. (17). Thus, in order to obtain the energy dissipated in the system W_{diss} from the energy balance, it remains to estimate the energy W_{ext} introduced to the building by the wind. During the measurement campaign, no wind sensors were installed on the building and, therefore, these data are not explicitly collected. However, the wind peak velocity and 1 h average velocity (Fig. 3) can be obtained in The Netherlands via the Royal Netherlands Meteorological Institute database. Using these data, in combination with a well-established procedure, a realistic wind energy spectrum can be computed as described below.

First, the wind pressure p_{wind} caused by the wind velocity normal to the face B of the building is computed. It is generally assumed that the wind velocity contains a mean component $\bar{v}(x)$ and a fluctuating component $\tilde{v}(x,t)$, both dependent on the height x

$$p_{\text{wind}}(x,t) = \frac{1}{2}\rho_w\left(\bar{v}(x) + \tilde{v}(x,t)\right)^2 \tag{19}$$

where ρ_w is the air density. The wind load per unit length of the building is equal to the wind pressure multiplied by the building width B and the shape factor C_f

$$q_{\text{wind}}(x,t) = \frac{1}{2}\rho_w B C_f\left(\bar{v}(x) + \tilde{v}(x,t)\right)^2 \tag{20}$$

Now, the rate of energy $\Xi_{\text{ext}}(x,t)$ introduced to the unit length of the building by the wind can be computed by multiplying the wind load q_{wind} by the velocity of the building. We assume that the wind blows in the weak direction (parallel to the y-axis) of the building. This result into the following expression for $\Xi_{\text{ext}}(x,t)$:

$$\Xi_{\text{ext}}(x,t) = \frac{1}{2}\rho_w C_f B\left(\bar{v}(x) + \tilde{v}(x,t)\right)^2 \dot{u}_y(x,t) \tag{21}$$

The fluctuating component of the wind velocity is significantly smaller than the mean velocity. And, the velocity of the building is also much smaller than the mean wind velocity [30]. Therefore, we will use the linearized version of Eq. (21), which can be written as follows:

$$\Xi_{\text{ext}}(x,t) = \frac{1}{2}\rho_w C_f B\bar{v}^2(x)\dot{u}_y(x,t) \tag{22}$$

The mean wind velocity is normally assumed to have a logarithmic variation along the building height. Therefore, according to Eurocode NEN-EN 1991-1-4, the mean wind velocity function can be described by the following expression:

$$\bar{v}(x) = 0.19\left(\frac{x_0}{x_{0,II}}\right)^{0.07}\ln\left(\frac{x}{x_0}\right)v_{b,0}, \tag{23}$$

where $v_{b,0} = 27$ m/s is the mean wind speed, $x_{0,\text{II}} = 0.05$ is a parameter that accounts for the location of the buildings, and $x_0 = 0.5$ accounts for the roughness of the terrain.

To obtain the total rate of energy introduced by the wind, Eq. (22) is integrated over the length of the superstructure as follows:

$$W_{\text{ext}}(\tilde{t}) = \int_0^L \Xi_{\text{ext}}(x,t)dx = \frac{1}{2}\rho_w C_f B\int_0^L \dot{u}_y(x,t)\bar{v}^2(x)dx \tag{24}$$

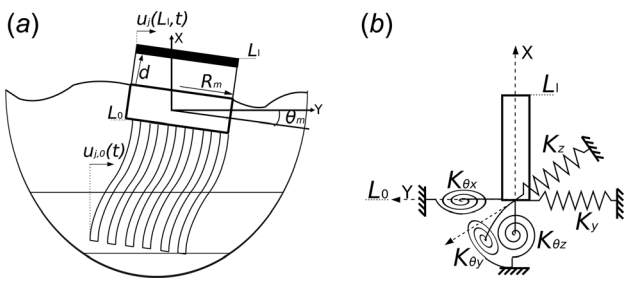

Fig. 8 Description of the soil foundation and low part of the building: (*a*) sketch of the soil foundation and low part of the building and (*b*) simplification of the soil foundation and low part of the building by means of a beam model and springs

Given that the velocity of the building is known only at the measurement locations, a linear approximation of the building velocity is used: $\dot{u}_y(x,t) = (\dot{u}_y(L_f,t) - \dot{u}_y(L_1,t)/L_f - L_1)x + \dot{u}_y(L_1,t)$.

At this point, W_{diss}, which accounts for the rate of energy dissipated at the superstructure, is the only unknown in the energy balance, Eq. (12). Therefore, the energy dissipated as a function of frequency can be also computed in accordance with Eq. (17).

3.3 Energy Dissipation in the Soil–Foundation Interaction of the JuBi Tower. Now, in order to compute the energy dissipation due to the SSI (W_{diss}^{SSI}), the recorded data at the bottom floor (9th floor) in combination with the energy balance equation are used. Strictly speaking with this choice of data (9th floor), the energy dissipation to be found does not only correspond to the soil foundation, since the part of the superstructure from the ground level to the 9th floor is included in the energy balance to find the energy dissipated. Ideally, measurements at ground level were desired; however, due to strict safety regulations, the 9th floor was the lowest level allowed to install equipment for measurements. Therefore, the energy dissipated will correspond to the SSI and the very lowest part of the superstructure. It is expected though that, due to a very high rigidity of the lower part of the building in comparison with the soil stiffness, the energy dissipated between the 9th floor and the ground level is significantly smaller than the energy dissipated in the soil–structure interaction.

Given that there is only acceleration and strain data recorded at the 9th floor, some assumptions need to be made in order to quantify the energy dissipation around the soil-foundation part. First, the lower part of the building, from the 9th floor to the ground level, is assumed to move as a rigid body. Second, the complex interaction between the soil and the building foundation is simplified by means of springs, which represent the dynamic stiffness of the soil–foundation interaction for the different directions as shown in Fig. 8.

Now, considering the model sketched in Fig. 8(*b*), the energy balance described in Eq. (12) can be used. $E(\tilde{t})|_t^{t+T}$ can be computed by means of the following equation:

$$E(\tilde{t})|_t^{t+T} = (L_l - L_0)\tilde{e}_1(\tilde{t})|_t^{t+T} \tag{25}$$

where $\tilde{e}_1(\tilde{t})$ was computed in the previous section. The energy flow $S(L_l,\tilde{t})$ is computed by means of Eq. (15). $S(L_0,\tilde{t})$ is set to zero given the fact that the soil–structure interaction is accounted for by the springs shown in Fig. 8(*b*). The rate of elastic energy related to soil–structure interaction can be computed as

$$W_{ext}(\tilde{t}) = K_y w_y(L_0,t)\dot{w}_y(L_0,t) + K_z w_z(L_0,t)\dot{w}_z(L_0,t)|_{L_0} + K_{\theta_y}\theta_y(L_0,t)\dot{\theta}_y(L_0,t) + K_{\theta_z}\theta_z(L_0,t)\dot{\theta}_z(L_0,t) + K_{\theta_x}\theta_x(L_0,t)\dot{\theta}_x(L_0,t) \tag{26}$$

The stiffnesses K_y, K_z, K_{θ_y}, K_{θ_z}, and K_{θ_x} are computed by means of the well-established software Dynapile. Realistic stiffness values are computed by introducing the soil profile described in Fig. 2, the pile plan, and the pile characteristics.

Now, the energy balance equation Eq. (17) contains only one unknown, the spectra of the energy dissipation, $\tilde{W}_{diss}(\omega) = \int_{-\infty}^{\infty}\int_t^{t+T} W_{diss}(\tilde{t})e^{-i\omega t}dtd\tilde{t}$, which can be computed.

4 Quantification of the Energy Dissipation in the JuBi Tower

Having computed all the terms of Eq. (17), but the energy dissipation $W_{diss}(\tilde{t})$, the spectra of the energy dissipation in the superstructure $\tilde{W}_{diss}^{structure}(\omega)$, and in the SSI $\tilde{W}_{diss}^{SSI}(\omega)$ can be calculated. The results of these calculations are plotted in Fig. 9.

Once the dissipated energy is identified, it is of interest to characterize the velocity dependence of the damping force that could cause this energy dissipation. Although a wide range of the velocity dependences can be thought of, three most widely used dependences are considered, namely the ones of the viscous type $\dot{u}(t)$, of the quadratic type $\dot{u}(t)|\dot{u}(t)|$ and of the hysteretic type $(\dot{u}(t)/|\dot{u}(t)|)$. The damping mechanisms are described by means of the damping forces as

$$F_{D_1}(t,x) = \sum_{i=1}^{3} F_{D_1}^i(t,x) = \sum_{i=1}^{3} C_1^i \dot{u}_i(t,x) \tag{27}$$

$$F_{D_2}(t,x) = \sum_{i=1}^{3} F_{D_1}^i(t,x) + \sum_{i=1}^{3} F_{D_2}^i(t,x) = \sum_{i=1}^{3} C_1^i \dot{u}_i(t,x) + \sum_{i=1}^{3} C_2^i \dot{u}_i(t,x)|\dot{u}_i(t,x)| \tag{28}$$

$$F_{D_3}(t,x) = \sum_{i=1}^{3} F_{D_1}^i(t,x) + \sum_{i=1}^{3} F_{D_3}^i(t,x) = \sum_{i=1}^{3} C_1^i \dot{u}_i(t,x) + \sum_{i=1}^{3} C_3^i \frac{\dot{u}_i(t,x)}{|\dot{u}_i(t,x)|} \tag{29}$$

where $F_{D_1}(t)$ is the linear damping force, $F_{D_2}(t)$ is the combination of the linear and the quadratic damping force, and $F_{D_3}(t)$ is the combination of the linear and the hysteretic damping force. The rate of the dissipated energy associated with these damping mechanisms can be written as

$$W_{diss_1}(t) = \sum_{i=1}^{3}\int_0^L F_{D_1}^i(t,x)\dot{u}_i(t,x)dx = \sum_{i=1}^{3} C_{1_i}^i \int_0^L \dot{u}_i^2(t,x)dx \tag{30}$$

$$W_{diss_2}(t) = \sum_{i=1}^{3}\int_0^L F_{D_1}^i(t,x)\dot{u}_i(t,x)dx + \sum_{i=1}^{3}\int_0^L F_{D_2}^i(t,x)(\dot{u}_i(t,x)|\dot{u}_i(t,x)|)dx = \sum_{i=1}^{3} C_1^i \int_0^L \dot{u}_i^2(t,x)dx + \sum_{i=1}^{3} C_2^i \int_0^L (\dot{u}_i^2(t,x)|\dot{u}_i(t,x)|)dx \tag{31}$$

$$W_{diss_3}(t) = \sum_{i=1}^{3}\int_0^L F_{D_1}^i(t,x)\dot{u}_i(t,x)dx + \sum_{i=1}^{3}\int_0^L F_{D_3}^i(t,x)\left(\frac{\dot{u}_i(t,x)}{|\dot{u}_i(t,x)|}\right)dx = \sum_{i=1}^{3} C_1^i \int_0^L \dot{u}_i^2(t,x)dx + \sum_{i=1}^{3} C_3^i \int_0^L \left(\frac{\dot{u}_i^2(t,x)}{|\dot{u}_i(t,x)|}\right)dx \tag{32}$$

In order to obtain the velocity dependence associated with the rate of energy dissipation in the superstructure, the following linear relation between the velocities measured at lowest and the top measurement points is assumed: $\dot{u}_i(x,t) = (\dot{u}_i(L_f,t) - \dot{u}_i(L_1,t)/L_f - L_1)x + \dot{u}_i(L_1,t)$. Since there is no measurement data recorded at the foundation, it is assumed that the velocity over the lowest part of the structure is constant. The spectra of the dissipation energy, where $\mathcal{F}$ designates the integral Fourier transform as defined in Eq. (16), are

$$\mathcal{F}(W_{diss_1}(t)) = \sum_{i=1}^{3} C_1^i \mathcal{F}\left\{\int_0^L \dot{u}_i^2(t,x)dx\right\} \tag{33}$$

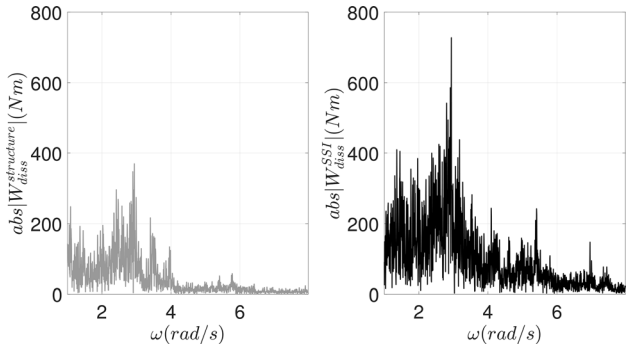

Fig. 9 The amplitude spectra of the dissipated energy in the JuBi tower subject to wind

$$\mathscr{F}(W_{\text{diss}_2}(t)) = \sum_{i=1}^{3} C_1^i \mathscr{F}\left\{\int_0^L \dot{u}_i^2(t,x)dx\right\} + \sum_{i=1}^{3} C_2^i \mathscr{F}\left\{\int_0^L \dot{u}_i^2(t,x)|\dot{u}_i(t,x)|dx\right\} \tag{34}$$

$$\mathscr{F}(W_{\text{diss}_3}(t)) = \sum_{i=1}^{3} C_1^i \mathscr{F}\left\{\int_0^L \dot{u}_i^2(t,x)dx\right\} + \sum_{i=1}^{3} C_3^i \mathscr{F}\left\{\int_0^L \frac{\dot{u}_i^2(t,x)}{|\dot{u}_i(t,x)|}dx\right\} \tag{35}$$

The spectra of the dissipated energy defined in Eq. (17) are related to the spectra defined by Eqs. (33)–(35) as

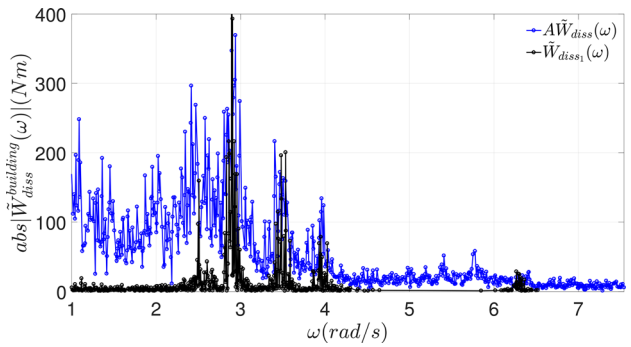

Fig. 10 Comparison of the linear damping to identify the energy dissipation of the superstructure

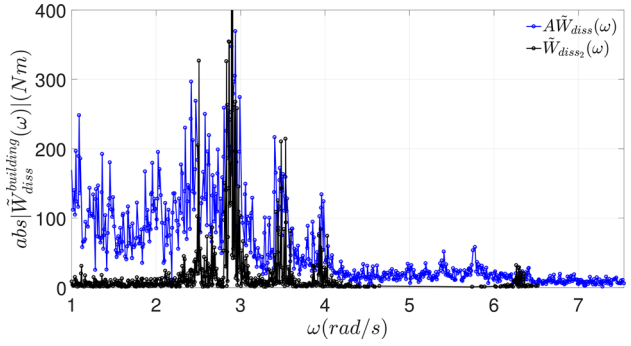

Fig. 11 Comparison of the quadratic damping to identify the energy dissipation of the superstructure

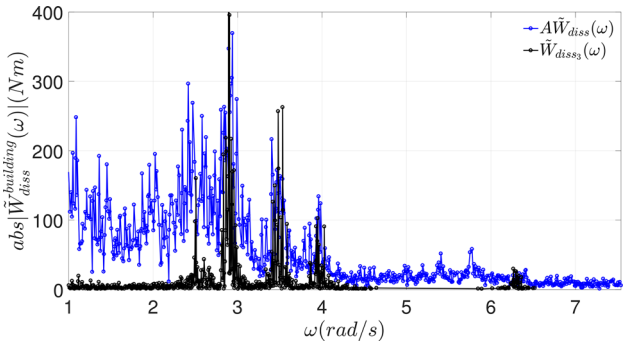

Fig. 12 Comparison of the hysteretic damping to identify the energy dissipation of the superstructure

$$\mathscr{F}(W_{\text{diss}_i}(t)) = A\tilde{W}_{\text{diss}}(\omega) \tag{36}$$

where,

$$A = \frac{2\pi\omega \mathrm{i}}{(e^{\mathrm{i}\omega T} - 1)} \tag{37}$$

is a frequency multiplier that accounts for the finite duration T of the measurement. The damping operator constants C_1^i, C_2^i, and C_3^i for each vibrational direction can be estimated by means of minimization of the mismatch in Eq. (36) as

$$\min_{C_i} \sum_{\omega_n} |\tilde{W}_{\text{diss}}(\omega) - \mathscr{F}(W_{\text{diss}_i}(t))| \text{ where } \omega_n = \Delta\omega n \tag{38}$$

Then, an estimate of the damping operator constant for the superstructure and the SSI associated with each vibration direction can be obtained. Using the damping constants obtained through the minimization procedure, the spectra of the dissipated energy corresponding to the three assumed dissipation forces can be obtained. These are shown in Figs. 10–15.

Figures 10–15 show the local maxima value of the spectra. The blue line represents the right-hand side of Eq. 36 and the black lines correspond to the energy dissipated predicted by the proposed damping mechanisms. Given the fact that C_1^i, C_2^i, and C_3^i are assumed to be constant, the minimization procedure has been carried out focusing on minimizing the error at the maxima of the spectra, which corresponds to the natural frequencies of the building within the measured frequency band. It can be pointed out that the energy dissipation $\tilde{W}_{\text{diss}_1}$, which corresponds to the energy dissipated obtained making use of the linear damping gives a reasonable approximation at the modal frequencies of the building. The energy dissipation predicted by the quadratic damping $\tilde{W}_{\text{diss}_2}$ gives a less accurate agreement at the natural frequencies. In this case study, the nonlinearity of the damping is not highly

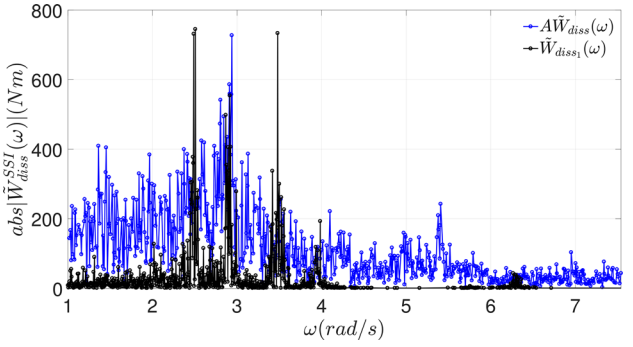

Fig. 13 Comparison of the linear damping to identify the energy dissipation of the SSI

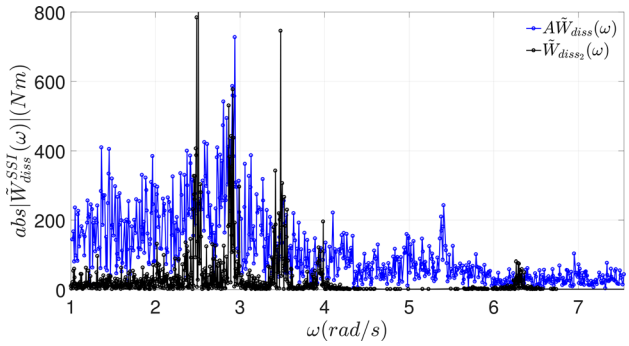

Fig. 14 Comparison of the quadratic damping to identify the energy dissipation of the SSI

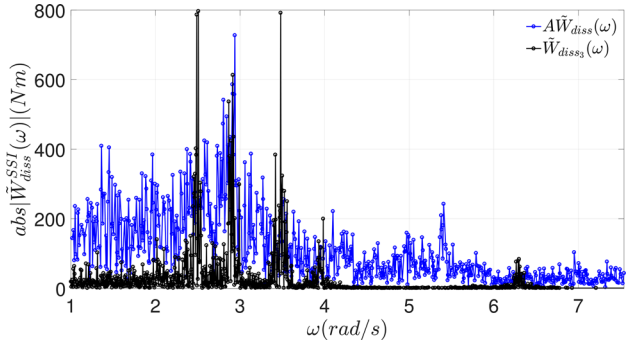

Fig. 15 Comparison of the hysteretic damping to identify the energy dissipation of the SSI

influential given the fact that the velocities are not large. The hysteretic damping mechanism $\tilde{W}_{\text{diss}_3}$ is the most sensitive to changes in the values of the constant. Therefore, the linear viscous damping force with the corresponding constants identified by means of the minimization will be used in Sec. 5.

5 Comparison of the Damping Identified by Means of the Energy Flow Analysis With the Measured Modal Damping

In order to validate the proposed energy method for damping identification, the equivalent damping ratios identified by means of the HPBW are compared to the computed modal damping ratios using the damping operators identified by means of the energy flow analysis. To this end, the model depicted in Fig. 16 is used. Equations of motion are given by Eqs. (8)–(10) assuming the cross-coupling terms to be negligible for simplification of the analysis. The boundary conditions are adopted from the foundation simplification depicted in Fig. 8, and C_{θ_m}, C_{θ_x}, $C_{\theta_m}^{\text{SSI}}$, and $C_{\theta_x}^{\text{SSI}}$ are the constants identified by means of the energy flow analysis.

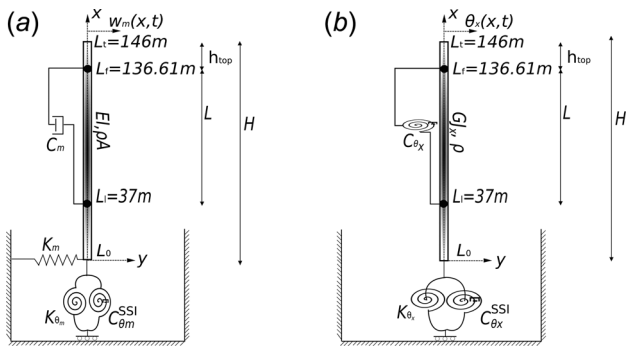

Fig. 16 One dimensional continuous model representative for a tall building including SSI effects: (*a*) bending beam model and (*b*) torsional beam model

Thus, EoMs that describe the small translational and torsional motions of the system in the Fourier domain are

$$-\omega^2\left(\sum_{k=1}^{N_{\text{cores}}}\rho_k A_k+\sum_{j=1}^{N_{\text{floors}}}\frac{M_j}{L}\right)\tilde{W}_m(x,\omega)+\sum_{k=1}^{N_{\text{cores}}}T_k\tilde{W}''_m(x,\omega)+\sum_{k=1}^{N_{\text{cores}}}EI_m^k\tilde{W}''''_m(x,\omega)=0 \tag{39}$$

where $m=y, z$, and

$$\omega^2\left(\sum_{k=1}^{N_{\text{cores}}}\rho J_0^k+\sum_{j=1}^{N_{\text{floors}}}\frac{M_j}{L}\right)\tilde{\theta}_x(x,\omega)+\sum_{k=1}^{N_{\text{cores}}}GJ_x^k\tilde{\theta}''_x(x,\omega)=0 \tag{40}$$

The boundary conditions at $x=L_0$ and $x=L_{\text{t}}$ are

$$\begin{aligned}
&\sum_{k=1}^{N_{\text{cores}}}EI_m^k\tilde{W}''_{m,1}(L_0,\omega)=(K_{\theta_m}+\text{i}\omega C_{\theta_m}^{\text{SSI}})\tilde{W}'_{m,1}(L_0,\omega)\\
&-\sum_{k=1}^{N_{\text{cores}}}EI_m^k\tilde{W}'''_{m,1}(L_0,\omega)=K_m\tilde{W}_{m,1}(L_0,\omega)\\
&\sum_{k=1}^{N_{\text{cores}}}EI_m^k\tilde{W}''_{m,3}(L_{\text{t}},\omega)=0\\
&\sum_{k=1}^{N_{\text{cores}}}EI_m^k\tilde{W}'''_{m,3}(L_{\text{t}},\omega)=0
\end{aligned} \tag{41}$$

$$\begin{aligned}
&\sum_{k=1}^{N_{\text{cores}}}GJ_x^k\theta'_x(L_0,\omega)=(K_{\theta_x}+\text{i}\omega C_{\theta_x}^{\text{SSI}})\tilde{\theta}_x(L_0,\omega)\\
&\sum_{k=1}^{N_{\text{cores}}}GJ_x^k\theta'_x(L_{\text{t}},\omega)=0
\end{aligned} \tag{42}$$

and the interface conditions at $x=L_{\text{l}}$ and $x=L_{\text{f}}$ are

Table 3 Identified parameters for the JuBi tower

		$m=y$	$m=z$
H(m)	146		
$\sum_{k=1}^{N_{\text{cores}}}EI_m^k$(Nm^2)		4.2e + 14	8.5e + 14
$\sum_{k=1}^{N_{\text{cores}}}\rho_k A_k+\sum_{j=1}^{N_{\text{floors}}}\frac{M_j}{L}$(Kg/m)	4.0e + 05		
K_m(N/m)		1.1e + 10	1.0e + 10
K_{θ_z}(Nm/rad)			5.25e + 12
K_{θ_y}(Nm/rad)		7.95e + 12	
$C_{\theta_z}^{\text{SSI}}$(Nms/rad)			3.5e + 10
$C_{\theta_y}^{\text{SSI}}$(Nms/rad)		6.0e + 10	
C_m(Ns/m)		5.0e + 05	1.6e + 06
$\sum_{k=1}^{N_{\text{cores}}}GJ_m^k$(Nm^2)	4.5e + 14		
C_{θ_x}(Nms/rad)	2.0e + 07		
K_{θ_x}(Nms/rad)	3.9e + 12		
$C_{\theta_x}^{\text{SSI}}$(Nms/rad)	2.1e + 10		

$$\sum_{k=1}^{N_{\text{cores}}} EI_m^k(\tilde{W}''_{m,2}(L_1,\omega) - \tilde{W}''_{m,1}(L_1,\omega)) = 0$$

$$-\sum_{k=1}^{N_{\text{cores}}} EI_m^k(\tilde{W}'''_{m,2}(L_1,\omega) - \tilde{W}'''_{m,1}(L_1,\omega)) = \mathrm{i}\omega C_m \tilde{W}_{m,1}(L_1,\omega)$$

$$\tilde{W}_{m,2}(L_1,t) = \tilde{W}_{m,1}(L_1,\omega)$$

$$\tilde{W}'_{m,2}(L_1,\omega) = \tilde{W}'_{m,1}(L_1,\omega)$$

$$\sum_{k=1}^{N_{\text{cores}}} EI_m^k(\tilde{W}''_{m,3}(L_f,\omega) - \tilde{W}''_{m,2}(L_f,\omega)) = 0$$

$$-\sum_{k=1}^{N_{\text{cores}}} EI_m^k(\tilde{W}'''_{m,3}(L_f,\omega) - \tilde{W}'''_{m,2}(L_f,\omega)) = \mathrm{i}\omega C_m \tilde{W}_{m,1}(L_f,\omega)$$

$$\tilde{W}_{m,3}(L_f,t) = \tilde{W}_{m,2}(L_f,\omega)$$

$$\tilde{W}'_{m,3}(L_f,\omega) = \tilde{W}'_{m,2}(L_f,\omega). \tag{43}$$

$$\sum_{k=1}^{N_{\text{cores}}} GJ_x^k(\tilde{\theta}'_{x,2}(L_1,\omega) - \tilde{\theta}'_{x,1}(L_1,\omega)) = \mathrm{i}\omega C_{\theta_x}^{\text{SSI}} \tilde{\theta}_{x,1}(L_1,\omega)$$

$$\tilde{\theta}_{x,1}(L_1,\omega) = \tilde{\theta}_{x,2}(L_1,\omega) \tag{44}$$

$$\sum_{k=1}^{N_{\text{cores}}} GJ_x^k(\tilde{\theta}'_{x,3}(L_f,\omega) - \tilde{\theta}'_{x,2}(L_f,\omega)) = \mathrm{i}\omega C_{\theta_x}^{\text{SSI}} \tilde{\theta}_{x,2}(L_f,\omega).$$

The equations of motion Eqs. (39) and (40), boundary and interface conditions Eqs. (41)–(44) are used to compute the following frequency equations Eqs. (45) and (46), whose roots are complex-valued natural frequencies of the system

$$det\mathbf{A}(\omega_n) = 0 \tag{45}$$

$$det\mathbf{B}(\omega_n) = 0 \tag{46}$$

Equation (45) is a 12×12 matrix, and Eq. (46) is a 6×6 matrix. The complex-valued natural frequencies are used to compute the equivalent modal damping ratio assuming single-degree-of-freedom dynamics by using the following expression:

$$\xi_i = \frac{\Im(\omega_n)}{\sqrt{\Re(\omega_n)^2 + \Im(\omega_n)^2}} \tag{47}$$

The parameters described in the model depicted in Fig. 16 are quantified using the values given in Table 3.

As already pointed out above, the stiffnesses K_y, K_z, K_{θ_y}, K_{θ_z} and K_{θ_x} shown in Table 3 are computed by means of the software Dynapile making use of the pile plan of the building and the soil profile. The bending stiffness EI_m and the torsional stiffness GJ_x are computed making use of the Young's modulus E and the shear modulus G corresponding to the building material, and the technical information to calculate the moments of inertia I_m and J_x. The mass per unit length ρA of the building is calculated using the density of the reinforce concrete material and the area of the cores and outer walls is obtained by means of the technical information provided in the drawings. The mass of the floors M_j is quantified making use of the technical information of the floors. Finally, the damping constant values C_m, C_{θ_x}, $C_{\theta_z}^{\text{SSI}}$, $C_{\theta_y}^{\text{SSI}}$ and $C_{\theta_x}^{\text{SSI}}$ are obtained by means of the energy flow analysis.

The resultant damping ratio associated with the translational and torsional modes is compared to the identified damping in Table 2.

Table 2 shows that the identified equivalent viscous damping values are slightly lower than the ones obtained with the energy flow analysis. However, this discrepancy is acceptable given the complexity of the structure. It is important to notice that the damping ratios shown in the right column (energy method) in Table 2 are the true modal damping ratios, while the experimentally identified damping ratios are just indicative due to the presence of the closely spaced modes that can be seen in Fig. 6. However, for low damped systems such as the JuBi tower, these damping ratios are close enough to the modal damping values. Moreover, the process of damping identification by means of the energy flow analysis contains some assumptions due to the complexity of the full-scale building system and the environment. Given that, the damping identification has led to inaccuracies. Nevertheless, it can be stated that the energy flow analysis establishes a consistent framework for damping identification.

6 Conclusions

In this paper, a new method based on an energy flow analysis for identification of damping in a selected part of a structure has been presented. A full-scale tall building located in the Netherlands has been chosen as an example to demonstrate the capabilities of the method. In accordance with this method, the energy balance of a selected part of the building is employed to identify the energy dissipated therein. In this work, the energy flow analysis has been applied to two parts of the building, namely to the superstructure and to the soil-foundation system. By doing so, the energy dissipated in the superstructure and in the soil-foundation system was identified independently of each other. Thanks to that, the relative contribution of damping in each part of the structure to the overall damping has been studied.

A quantification of damping in selected parts of a building is important in view of potential design improvement that will allow for the reduction of the accelerations of building subject to the dynamic loads. It has been shown in this paper that this method also enables identification of a damping mechanism that mimics the energy dissipated of the building.

The damping constants associated with the dissipation in the superstructure and in the soil-foundation system identified by means of the energy flow analysis have been validated in this paper using a model that takes into account the soil–structure interaction effects.

Appendix: Assumptions

The assumptions used in this paper to compute the energy dissipation in the superstructure and in the SSI are listed below. And, the reasons for the validity of these assumptions are also given.

- The assumption used in Eq. (1) in Sec. 2.3 is because in the frequency range that the building vibrates due to the wind loading (0–3 Hz), only global modes of the building are excited. Therefore, in-plane deformation of the floors is not expected.
- In Sec. 3.1 an Euler–Bernoulli beam model is used as to interpret the energy flow analysis. Coupling effects are taking into account in this model as shown in Eq. (3).
- In order to compute the energy change described in Eqs. (18)–(25), few assumptions were taken. First, the energy flow and the potential energy at the top are assumed to be negligible compared to the kinetic energy. The reason to assume this is because the potential energy of the building decreases with the distance from the foundation, just like in the cantilever beam, it decreases with the distance from the clamp. At the top level this energy, due to a very low bending and shear, it is much smaller than the kinetic energy (the latter is maximal at the top in the fundamental mode of vibration), which forms the basis for neglecting the potential energy in comparison with the kinetic one. As to the energy flow, one can put forward the following justification. The energy flow through the roof is zero. Therefore, as the energy flow must be a continuous function of the coordinate, it has to be small also in the close vicinity of the roof. This is why

the energy flow through the top level is neglected. Finally, Eqs. (18)–(25) are computed as an averaged value over the height of the building given that data are collected at two heights of the structure.

- The assumption of using a constant velocity over the low part of the building (from the 9th floor to the ground level) is taken because of the following reason. The lower part of the building is attached to a low-rise structure that is very stiff in the horizontal directions (Y- and Z-directions). It is much stiffer than the soil. Therefore, it is reasonable to assume that the lower part of the building will move horizontally as a rigid body thereby having a constant horizontal velocity over its height.

References

[1] Jeary, A. P., 1986, "Damping in Tall Buildings-a Mechanism and a Predictor," Earthquake Eng. Struct. Dyn., **14**(5), pp. 733–750.
[2] Lagomarsino, S., 1993, "Forecast Models for Damping and Vibration Periods of Buildings," J. Wind Eng. Ind. Aerodyn., **48**(2–3), pp. 221–239.
[3] Tamura, Y., Satake, N., Arakawa, T., and Sasaki, A., 2003, "Damping Evaluation Using Full-Scale Data of Buildings in Japan," J. Struct. Eng., **129**(4), pp. 470–477.
[4] Davenport, A., and Caroll, P. H., 1986, "Damping in Tall Buildings: Its Variability and Treatment in Design," ASCE Spring Convention, Seattle, WA, pp. 42–57.
[5] Ewins, D., 2000, *Modal Testing: Theory, Practice and Application*, Research Studies Press, Hertfordsire, UK.
[6] Peeters, B., and Roeck, G. D., 2001, "Stochastic System Identification for Operational Modal Analysis: A Review," ASME J. Dyn. Syst., Meas. Control, **123**(4), pp. 659–667.
[7] He, J., and Fu, Z.-F., 2001, *Modal Analysis*, Butterworth-Heinemann, Oxford, UK.
[8] Gómez, S. S., Metrikine, A., Carboni, B., and Lacarbonara, W., 2017, "Identification of Energy Dissipation in Structural Joints by Means of the Energy Flow Analysis," ASME J. Vib. Acoust., **140**(1), p. 011007.
[9] Gómez, S., and Metrekine, A., 2017, "Evaluation of the Applicability of an Energy Method to Calculate the Damping in a Lab-Scale Structure," Procedia Engineering: X International Conference on Structural Dynamics (EURODYN), Vol. 199, pp. 459–464.
[10] Wohlever, J., and Bernhard, R., 1992, "Mechanical Energy Flow Models of Rods and Beams," J. Sound Vib., **153**(1), pp. 1–19.
[11] Wickert, J. A., and Mote, C., 1989, "On the Energetics of Axially Moving Continua," J. Acoust. Soc. Am., **85**(3), pp. 1365–1368.
[12] Barakat, R., 1968, "Transverse Vibrations of a Moving Thin Rod," J. Acoust. Soc. Am., **43**(3), pp. 533–539.
[13] Lase, Y., Ichchou, M., and Jezequel, L., 1996, "Energy Flow Analysis of Bars and Beams: Theoretical Formulations," J. Sound Vib., **192**(1), pp. 281–305.
[14] Bouthier, O., and Bernhard, R., 1995, "Simple Models of the Energetics of Transversely Vibrating Plates," J. Sound Vib., **182**(1), pp. 149–164.
[15] Han, F., Bernhard, R., and Mongeau, L., 1997, "Energy Flow Analysis of Vibrating Beams and Plates for Discrete Random Excitations," J. Sound Vib., **208**(5), pp. 841–859.
[16] Lebot, A., and Jezequel, L., 1993, "Energy Methods Applied to Transverse Vibrations of Beams," Fourth International Congress on Intensity Techniques, pp. 371–378.
[17] Pinnington, R., and Lednik, D., 1996, "Transient Energy Flow Between Two Coupled Beams," J. Sound Vib., **189**(2), pp. 265–287.
[18] Alfredsson, K., 1997, "Active and Reactive Structural Energy Flow," ASME J. Vib. Acoust., **119**(1), pp. 70–79.
[19] Sorokin, S., Nielsen, J., and Olhoff, N., 2001, "Analysis and Optimization of Energy Flows in Structures Composed of Beam Elements–Part I: Problem Formulation and Solution Technique," Struct. Multidiscip. Optim., **22**(1), pp. 3–11.
[20] Bouthier, O., and Bernhard, R., 1995, "Simple Models of Energy Flow in Vibrating Membranes," J. Sound Vib., **182**(1), pp. 129–147.
[21] Hegazy, Y. A., and Mayne, 1995, "Statistical Correlations Between Vs and Cone Penetration Data for Different Soil Types," Paper No. A87.
[22] Mayne, P. W., and Rix, G. J., 1995, "Correlations Between Shear Wave Velocity and Cone Tip Resistance in Natural Clays," Soils Foundations, **35**(2), pp. 107–110.
[23] Andrus, R. D., Mohanan, N. P., Piratheepan, P., Ellis, B., and Holzer, T. L., 2007, "Predicting Shear-Wave Velocity From Cone Penetration Resistance," Fourth International Conference on Earthquake Geotechnical Engineering, Thessaloniki, Greece, June 25–28.
[24] Robertson, P. K., 2009, "Interpretation of Cone Penetration Tests—A Unified Approach," Can. Geotech. J., **46**(11), pp. 1337–1355.
[25] Papagiannopoulos, G. A., and Hatzigeorgiou, G. D., 2011, "On the Use of the Half-Power Bandwidth Method to Estimate Damping in Building Structures," Soil Dyn. Earthquake Eng., **31**(7), pp. 1075–1079.
[26] Ellis, B., 1986, "The Significance of Dynamic Soil-Structure Interaction in Tall Buildings," Ice Proc., **81**(2), pp. 221–242.Vol.
[27] Kausel, E., 2010, "Early History of Soil-Structure Interaction," Soil Dyn. Earthquake Eng., **30**(9), pp. 822–832.
[28] Novak, M., 1974, "Dynamic Stiffness and Damping of Piles," Can. Geotech. J., **11**(4), pp. 574–598.
[29] Gazetas, G., and Makris, N., 1991, "Dynamic Pile-Soil-Pile Interaction. part i: Analysis of Axial Vibration," Earthquake Eng. Struct. Dyn., **20**(2), pp. 115–132.
[30] Balendra, T., 1993, *Vibration of Buildings to Wind and Earthquake Loads*, Springer-Verlag, London.